Stratiform cloud electrification: comparison of theory with multiple in-cloud measurements

RMetS
Royal Meteorological Society

Stratiform cloud electrification: comparison of theory with multiple in-cloud measurements

K. A. Nicoll* and R. G. Harrison
Department of Meteorology, University of Reading, UK

*Correspondence to: K. A. Nicoll, Department of Meteorology, University of Reading, Whiteknights Campus, Reading, Berkshire RG6 6BB, UK. E-mail: k.a.nicoll@reading.ac.uk

Stratiform clouds constitute ∼40% of global cloud cover and play a key role in determining the planetary radiation budget. Electrification remains one of the least understood effects on their microphysical processes. Droplet charging at the top and bottom edges of stratiform clouds arises from vertical current flow through clouds driven by the Global atmospheric Electric Circuit. In-cloud charge data are central in assessing the role of charge in droplet growth processes, which influence droplet size distributions and associated cloud radiative properties and precipitation. This study presents the first high vertical resolution electrical measurements made in multiple layer clouds. Of the 22 clouds sampled, all were charged at their edges, demonstrating unequivocally that all stratiform clouds can be expected to contain charge at their upper and lower boundaries to varying extent. Cloud base and cloud top are shown to charge asymmetrically, with mean cloud-top space charge $+32\,\mathrm{pC\,m^{-3}}$ and base space charge $-24\,\mathrm{pC\,m^{-3}}$. The larger cloud-top charges are associated with strong temperature inversions and large vertical electrical conductivity gradients at the upper cloud boundary. Greater charging was observed in low altitude (<2 km) clouds ($20.2\,\mathrm{pC\,m^{-3}}$), compared to higher altitude (>2 km) cloud layers ($7.0\,\mathrm{pC\,m^{-3}}$), consistent with the smaller air conductivity at lower altitudes associated with reduced cosmic ray ionisation. Taken together, these measurements show that the greatest cloud droplet charges in extensive stratiform clouds occur at cloud tops for low altitude (<2 km) clouds, when vertical mixing is suppressed by appreciable temperature inversions, confirming theoretical expectations. The influence of cloud dynamics on layer cloud edge charging reported here should inform modelling studies of cloud droplet charging effects on cloud microphysics.

Key Words: atmospheric electricity; balloon meaurements; radiosonde; cloud electricity

Received 12 February 2016; Revised 11 May 2016; Accepted 13 June 2016; Published online in Wiley Online Library

1. Introduction

Earth's atmosphere is a weak conductor of electricity due to the presence of atmospheric cluster ions, formed, near the surface, from natural radioactivity in rock and soil, and at higher altitudes by Galactic Cosmic Rays (GCRs). GCRs are the primary source of ionisation above the Earth's surface, creating a cascade of charged energetic particles by collision with O_2 and N_2 molecules as they enter the atmosphere from above. The presence of cluster ions, and the existence of a Global atmospheric Electric Circuit (GEC) permit a small current density, J_c, ($\sim 10^{-12}\,\mathrm{A\,m^{-2}}$) to flow vertically from the lower ionosphere (approx. 60 km altitude) to Earth's surface (e.g. Wilson, 1929; Israel, 1971). This provides a link between the upper atmosphere and the lower troposphere, in all fair-weather regions of the globe. Conventional atmospheric electricity (e.g. Israel, 1971) distinguishes between disturbed weather (i.e. thunderstorm conditions) and fair-weather regions (where there is no local charge generation), but there also exists a very common, but seldom mentioned, situation of semi-fair weather conditions – defined here as conditions pertaining to extensive, non-precipitating layer clouds. These are different from electrified shower clouds which, like thunderstorms, contribute significantly to the GEC current flow (e.g. Mach *et al.*, 2011; Blakeslee *et al.*, 2014) and are typically associated with precipitation. Layer clouds are prevalent, covering almost 40% of the planet's surface at any one time (Klein and Hartmann, 1993), and play a large role in the terrestrial radiation balance. When such extensive clouds are present, the fair-weather current must pass through the cloud (experimentally verified by Bennett and Harrison (2009) and Nicoll and Harrison (2009b); modelled by Baumgaertner *et al.* (2014)). The consequence of current flow through cloud layers is for charge accumulation to occur at the top and bottom horizontal cloud edges (Tinsley, 2000; Zhou and Tinsley, 2007), due to the conductivity transition between the clear air and cloudy regions (see e.g. Harrison *et al.* (2015), Figure 1). We define the horizontal cloud edge here as the transition that occurs between cloud and cloud-free air at the cloud base or top (not the sides of the cloud).

Charging of cloud droplets has implications for their behaviour and can affect cloud microphysical processes such as droplet–droplet interactions (e.g. Khain *et al.*, 2004), aerosol–droplet interactions (e.g. Tinsley *et al.*, 2000) and droplet activation (e.g. Harrison and Ambaum, 2008). Harrison *et al.* (2015) discuss these mechanisms in detail. The magnitude of cloud droplet charge required to affect each of these cloud microphysical processes varies between a few electronic charges to a few thousand, depending on the process and the droplet size. The likely large-scale effect of charge on the cloud droplet population is a change in size or number concentration of the droplets, which can lead to a change in the radiative properties of the cloud, and potentially precipitation changes. This is supported by recent observations of changes in cloud-base properties associated with well-known atmospheric electrical variations (Harrison and Ambaum, 2013; Harrison *et al.*, 2013). As stratus clouds are common globally (being particularly prevalent over oceanic regions) (Klein and Hartmann, 1993), and the vertical current is always present in semi-fair weather regions, electrical microphysical effects may provide an underlying source of variability in cloud properties.

Characterisation of the typical droplet charge in layer clouds is a key factor in understanding cloud-edge electrical effects, and is at present not well known. Previous measurements of cloud droplet charging in non-thunderstorm cloud have mostly been made from mountaintop observatories in the 1950s (e.g. Twomey, 1956; Phillips and Kinzer, 1958; Allee and Phillips, 1959), where droplet charges of typically ±20 elementary charges (e) were found (Phillips and Kinzer, 1958). There remain, however, concerns that the electrical conditions at mountaintops are not representative of meteorological conditions in clouds in the free atmosphere. Aircraft measurements of droplet charging were made by Beard *et al.* (2004) within altostratus, although charge measurements were only reported for the middle of the cloud rather than on the upper and lower edges, where the charge accumulates. In the United Kingdom, balloon-borne measurements by Jones (1957) and Jones *et al.* (1959) demonstrated appreciable gradients in electric field and conductivity at horizontal cloud edges inside a stratiform cloud layer, whilst half a century later Nicoll and Harrison (2010) reported high vertical resolution charge measurements from a similar free balloon platform through a layer of stratocumulus cloud. A region of negative charge (up to $-35\,\mathrm{pC\,m^{-3}}$) was found at cloud base, with a magnitude similar to that predicted by theory. These sparse measurements confirmed the existence of charging at upper and lower edges of layer clouds; however, further quantitative study of the location, polarity and magnitude of charge carried by cloud droplets in layer clouds is required to inform modelling studies of charge influences on cloud microphysical processes.

This article presents a unique new dataset of observations of layer cloud charging at horizontal edges using specially designed charge and cloud instrumentation flown from free balloon platforms. Quantitative analysis of the electrical characteristics of a large number of stratiform cloud layers is reported, providing a new dataset with which to better understand the role of electrification in layer clouds. In section 2 the theory behind accumulation of charge on cloud edges is discussed, whilst in section 3 the instrumentation is described. Section 4 presents new measurements of edge charging for multiple clouds, and section 5 discusses the various factors controlling cloud-edge charging in terms of the measurements obtained. Section 6 discusses estimates of individual cloud-droplet charges, whilst section 7 includes a discussion and section 8 presents the conclusions.

2. Separation of charge at edges of extensive layer clouds

Charge accumulation is associated with the upper and lower horizontal edges of layer cloud due to the transition in electrical conductivity, σ_t, between clear air and droplet-laden air. Droplet-laden air has a lower conductivity (i.e. higher resistivity) than clear air due to the attachment of cluster ions (typically nm diameter) to the cloud droplets (typically μm diameter). The horizontal cloud-edge boundary region therefore has an associated vertical gradient in conductivity, with, in turn, a vertical gradient in the electric field, E. From Gauss' law of electrostatics, the change in the vertical component of the electric field E_z gives rise to a region of space charge of density ρ (defined as the net difference between positive and negative charge per unit volume):

$$\frac{dE_z}{dz} = -\frac{\rho}{\varepsilon_0}, \tag{1}$$

where ε_0 is the permittivity of free space and z is positive upwards. Assuming Ohm's law in the vertical direction, and expressing E_z in terms of conductivity σ_t(where the subscript t denotes the total conductivity, i.e. the contribution from both positive and negative conductivities), and the atmospheric potential gradient, PG, where $PG = -E_z$ and

$$J_c = \sigma_t PG, \tag{2}$$

it follows that Eq. (1) can be rewritten to give ρ in terms of the fair-weather conduction current density, J_c, as

$$\rho = -\varepsilon_0 J_c \frac{\mathrm{d}}{\mathrm{d}z}\left(\frac{1}{\sigma_t}\right) = -\varepsilon_0 J_c \frac{1}{{\sigma_t}^2}\left(\frac{\mathrm{d}\sigma_t}{\mathrm{d}z}\right). \tag{3}$$

The electrical changes which occur across a layer cloud are illustrated conceptually in Figure 1, for an assumed conductivity gradient at the upper and lower horizontal cloud boundaries. If the gradient is made sharper, a larger amount of space charge but over a narrower layer results. As will become apparent, this example is very much that of an idealised cloud layer.

The polarity of the charge layers generated by the vertical conductivity change is, accordingly, positive at the top and negative at the base of the cloud, due to the difference in the direction of the vertical conductivity gradients between the upper and lower cloud edges and the downward direction of the current flow. From the instant that cloud droplets start to form, a vertical gradient in conductivity will become established and charge will accumulate in these regions. The horizontal charge layers created at upper and lower horizontal cloud boundaries are maintained by the current flow through the cloud, which ensures a continuous supply of ions into the top and bottom of the cloud.

It is clear from Eq. (3) that cloud-edge charging depends on the vertical conductivity gradient which will be determined by local meteorological conditions, as well as the fair-weather current density, J_c. It follows that modulation of J_c, either from external sources such as GCR flux changes due to the solar magnetic field, or internal sources such as a change in thunderstorm generators in the GEC, will also modulate the space charge (e.g. Mach *et al.*, 2011; Nicoll, 2014). This is discussed in more detail in section 7. A further consideration, as pointed out by Harrison *et al.* (2015) is the variations with height which occur in the cosmic ray ion production rate and therefore in σ_t. The associated expectation is that the cloud-edge charging will vary with the height dependence in σ_t, assuming similar vertical profiles in the cloud droplet properties at different heights.

3. Methodology

3.1. Cloud and charge instrumentation

To estimate the typical charges on cloud droplets, knowledge of both the *in situ* cloud properties and charge profiles are required. A meteorological radiosonde provides a suitable platform with a typical vertical sampling resolution of ∼5 m from its ascent rate of $\sim 5\,\mathrm{m\,s^{-1}}$ and sampling rate of 1 Hz. The standard radiosonde only measures pressure, temperature, relative humidity (PTU) and position; however, a specially developed data acquisition

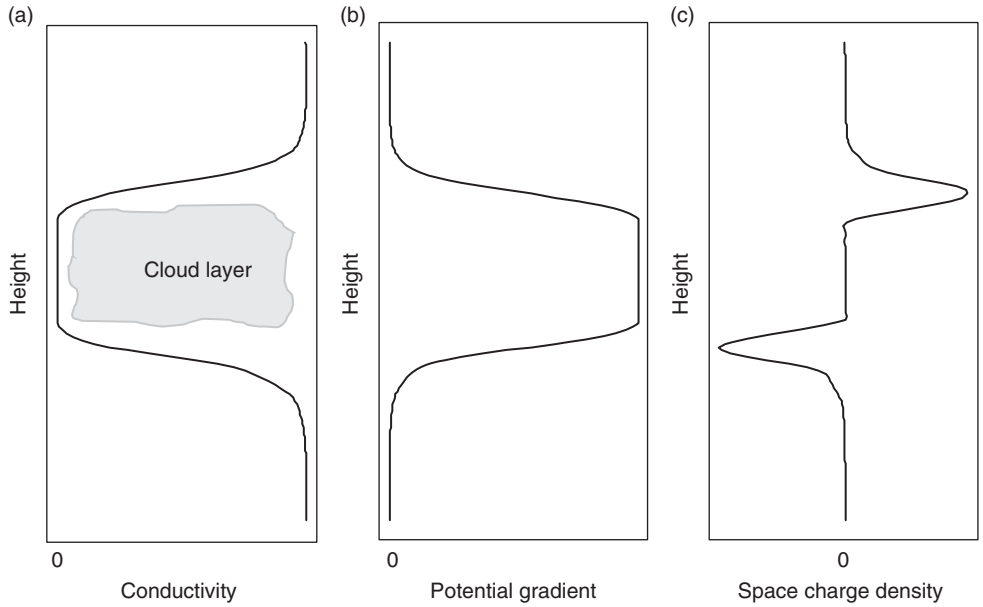

Figure 1. Hypothetical vertical profiles of atmospheric electrical quantities through a horizontally extensive stratiform cloud layer: (a) conductivity, (b) potential gradient, and (c) derived space-charge density.

system known as Programmable ANd Digital Operational Radiosonde Accessory (PANDORA: Harrison *et al.*, 2012) allows the attachment of additional science sensors, and transmission of the data synchronously with the PTU data. Adopting this approach, an optical cloud-droplet sensor has been developed to provide information on the cloud-droplet profile and determine the thickness of the cloud to clear-air transition (which is generally not well studied, either at horizontal cloud edges or vertical ones, as the so-called 'twilight zone' demonstrates (Koren *et al.*, 2007)). The sensor employs a backscatter method using an ultra-bright Light Emitting Diode (LED) at 590 nm as the source, with a photodiode receiver (Harrison and Nicoll, 2014). The cloud droplet sensor returns a measurement of visible range, X_r, which shows considerable change at the cloud-edge boundary (which occurs in the same region as the conductivity changes). The photodiode also provides a direct measurement of solar radiation, which provides a further independent determination of the cloud-edge boundary region in daylight (Nicoll and Harrison, 2012). In addition, a small charge sensor is flown alongside the optical cloud-droplet sensor to measure the net space-charge density within the cloud layer. This employs a spherical electrode connected to a sensitive electrometer. It primarily responds to induced displacement currents generated by electric field changes as the sensor moves through the cloud layer (Nicoll, 2013). Details of the space-charge derivation from the measurement of charge-sensor current are given in the Appendix. The combined package of the PANDORA, optical cloud droplet sensor and charge sensor has a mass of 250 g and is attached to the side of a standard Vaisala RS92 radiosonde, all flown under a 200 g helium-filled carrier balloon.

A useful comparison can be made between the space-charge profile measured by the charge sensor and that calculated from theory. This can be achieved from the data measured by the cloud-droplet sensor, which can be used to estimate the vertical in-cloud conductivity profile, and Eq. (3). To estimate the conductivity profile one must first consider the droplet concentration profile through the cloud layer. The cloud-droplet sensor was laboratory calibrated to provide optical extinction, ξ, by measuring the transmission of LED light through a region of droplet-laden air simultaneous with the optical backscatter (Harrison and Nicoll, 2014). The optical extinction is related to the visual range, X_r, by

$$X_r = \frac{\ln \varepsilon}{\xi}, \tag{4}$$

where ε is normally taken to be 0.05 (HMSO, 1982) (e.g. Harrison, 2012). Assuming an optical extinction coefficient for cloud droplets of approximately twice their projected area (e.g. Bohren and Huffman, 1983; Harrison, 2012), the total extinction coefficient ξ is related to the droplet diameter, d, and droplet number concentration, Z_d by

$$Z_d = \frac{2\xi}{\pi d^2}. \tag{5}$$

Thus, by assuming an average cloud droplet diameter (taken here to be 10 μm – a typical cloud droplet size for stratocumulus cloud (Miles *et al.*, 2000)), Z_d can be estimated. The cloud-droplet number concentration is a key parameter in calculating the conductivity profile through the cloud layer. Using the steady-state ion-balance equation (e.g. Harrison and Carslaw, 2003), which characterises the ion concentration in the presence of cloud droplets, the total conductivity is

$$\sigma_t = \frac{\mu e}{\alpha}\left(\sqrt{(\beta_a{}^2 Z_a{}^2 + 2\beta_a Z_a \beta_d Z_d + \beta_d{}^2 Z_d{}^2 + 4\alpha q_i)} - (\beta_a Z_a + \beta_d Z_d)\right), \tag{6}$$

where μ is the mean ion mobility (taken here as $1.7 \times 10^{-4}\,\mathrm{m^{-2}\,V^{-1}\,s^{-1}}$), e the elementary charge (1.6×10^{-19} C), $\alpha\,\mathrm{m^3\,s^{-1}}$ the ion–ion recombination coefficient ($1.6 \times 10^{-12}\,\mathrm{m^{-3}\,s^{-1}}$), Z_a the background aerosol number concentration (assumed here to be $1000\,\mathrm{cm^{-3}}$), and β_a and β_d the size-dependent ion–aerosol and ion–droplet attachment coefficients respectively (Gunn, 1954). Equation (6) assumes that the bipolar ion concentrations are equal and represents the cloud droplets by a single (monodisperse) size. q_i is the ion production rate per unit volume (typically 2 ion pairs $\mathrm{cm^{-3}\,s^{-1}}$ near the surface) which is described in more detail in the following paragraph. There is likely to be considerable variability in many of the parameters in Eq. (6) in real cloud environments, particularly in terms of Z_a and the mean aerosol radius, on which β_a depends, therefore a considerable range of values for σ_t is expected. Application of Eqs (4)–(6) to the cloud droplet sensor data allows the estimation of σ_t from the optical sensor, which can be applied to Eq. (3) to derive an estimate of the in-cloud space charge.

3.2. *Ionisation instrumentation*

Equation (6) demonstrates that knowledge of the ion production rate, q_i, is required to derive the conductivity. Using additional

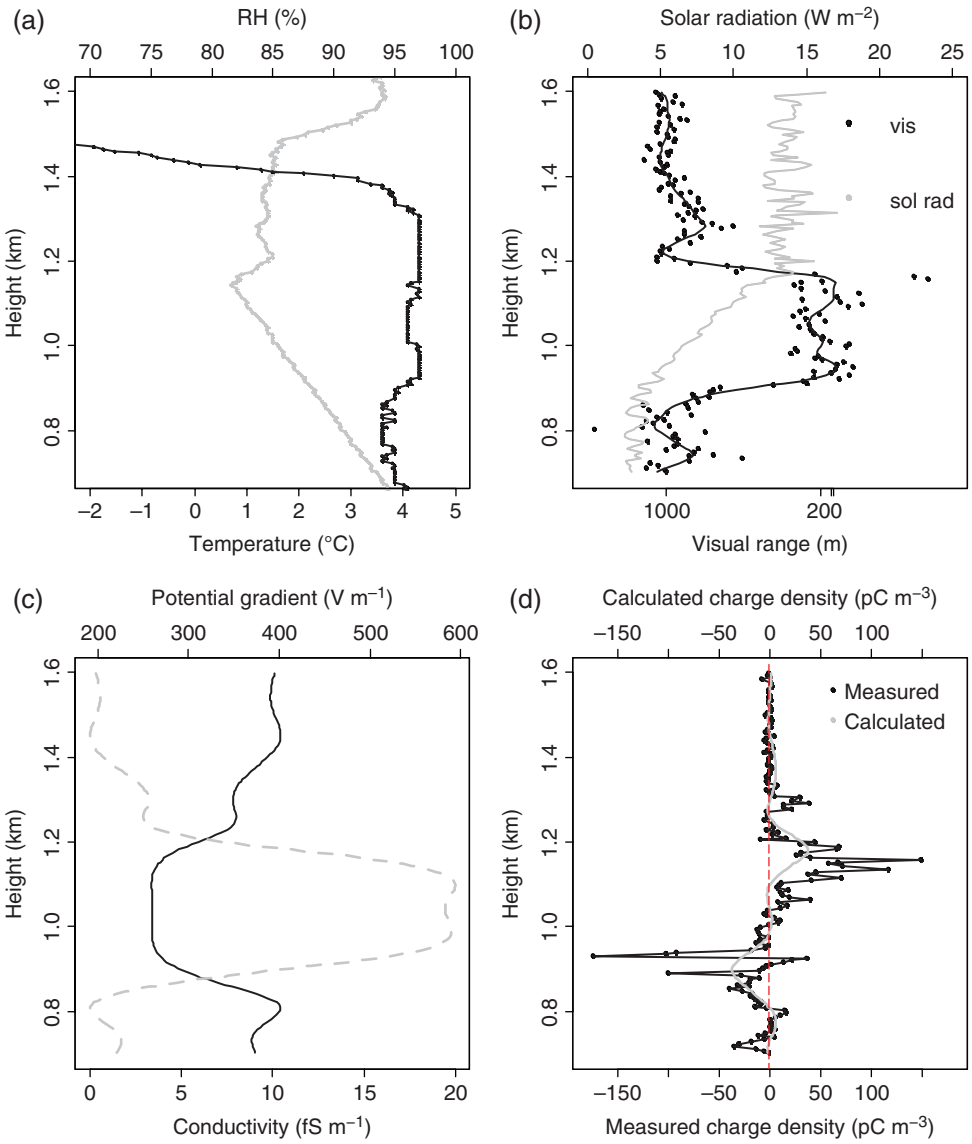

Figure 2. Vertical profile through a stratocumulus layer over Reading University Atmospheric Observatory (RUAO) from a specially instrumented radiosonde. (a) Temperature (grey) and relative humidity (RH) (black) measured by the radiosonde, (b) visual range and downwards solar radiation measured by an optical cloud-droplet sensor, (c) derived parameters of electrical conductivity (black) and potential gradient (grey dotted line) using Eqs (2) and (4)–(6) and assumptions outlined in section 3.1, and (d) space-charge density measured by a charge sensor (black line and data points) plotted alongside the expected space charge (grey line) calculated from the cloud-droplet sensor measurements using the theory in section 3.1.

instrumentation to detect the vertical profile of ionisation, q_i was measured directly on some of the charged-cloud flights. This approach uses two Geiger tubes (LND714) with a compact high-tension voltage supply, and an interval timing technique for improved resolution at low count rates (described by Harrison *et al.* (2013)). The electrical conductivity of air depends directly on the ion production rate, which varies as a function of altitude and latitude, and plays a role in determining the cloud-edge charge through Eq. (3). Over land, near the surface, ions are generated from natural radioactivity such as radon gas (4–8 ion pairs cm^{-3} s^{-1}: Hirsikko *et al.*, 2007), which are typically lofted to altitudes of 1–2 km within the atmospheric boundary layer. Galactic Cosmic Rays (GCRs) provide an additional source of ionisation of around 2 ion pairs cm^{-3} s^{-1} at the surface, which increases approximately exponentially with altitude to become the dominant ion source, reaching a maximum (the Regener–Pfotzer maximum) at ∼20 km (e.g. Bazilevskaya *et al.*, 2008). A consequence of the increase in ion production rate means that the conductivity also increases with height from a few fS m^{-1} at the surface to a few pS m^{-1} at 20 km. From Eq. (3), the space charge generated at cloud edges is proportional to $1/\sigma_t^2$, therefore, since σ_t varies with height, ρ is also expected to vary. This prediction is tested in section 5 using the measurements of ionisation rate obtained from the balloon Geiger sensor.

4. Charged cloud measurements

4.1. *Typical stratiform cloud*

To investigate layer-cloud charging, a series of specially instrumented balloon flights were carried out during 2013–2015, primarily from the Reading University Atmospheric Observatory (RUAO), United Kingdom (51.44°N, 0.95°W), but also from Hyytiala, Finland (61.85°N, 24.30°E), and Halley, Antarctica (75.35°S, 26.66°W). Low altitude non-frontal stratus and stratocumulus clouds of large horizontal extent (8/8ths cloud cover from a single site) were targeted since cloud-edge charging is expected from theory to be at its greatest with sharp cloud boundaries which require little vertical mixing, and at low altitudes (<5 km) where σ_t has its smallest values.

Figure 2 shows data from an instrumented balloon flight through stratocumulus cloud over RUAO on 18 November 2013, which had properties typical of stratiform cloud at Reading. From the thermodynamic measurements measured by the radiosonde (Figure 2(a)), the temperature inversion at 1.2 km indicates the cloud top; however, combined with the RH determination, the position of the cloud base is much more ambiguous. In contrast, both the optical cloud droplet (Figure 2(b)) and charge sensor (Figure 2(d)) show the cloud boundary regions very distinctly,

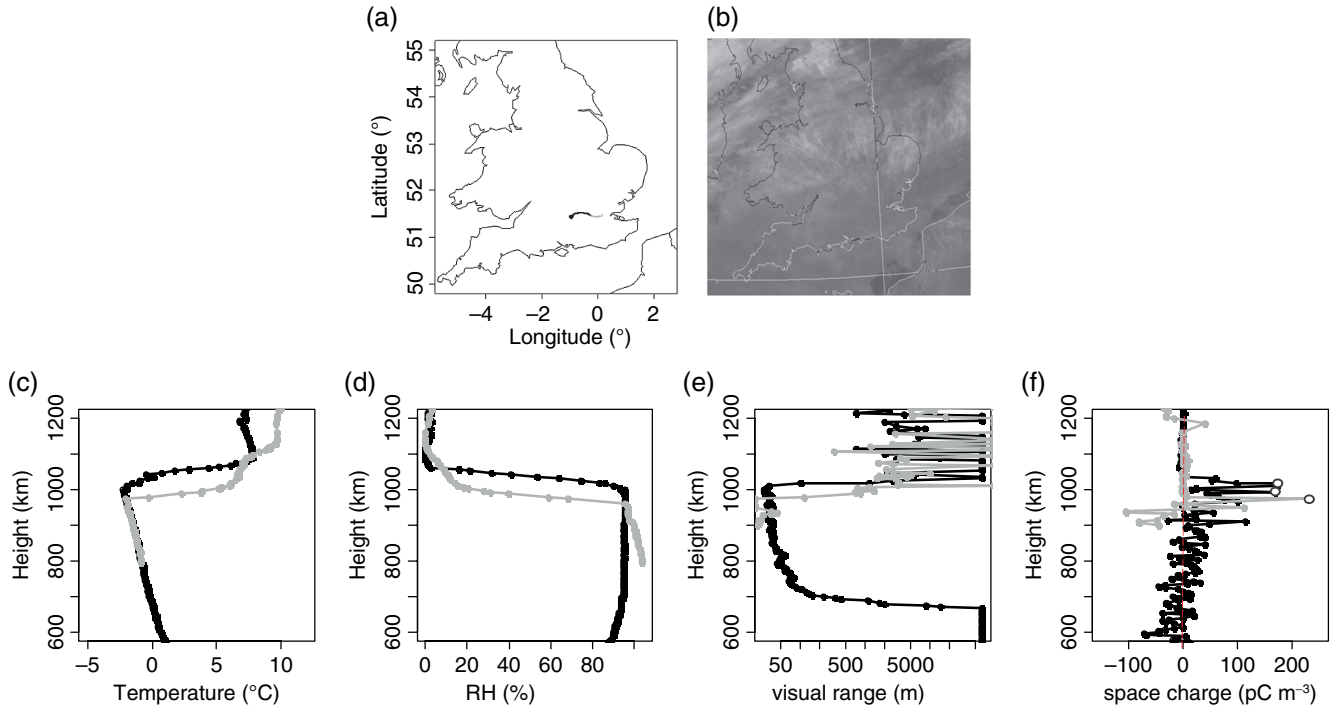

Figure 3. Ascent and descent of an instrumented balloon flight through the same cloud layer on 3 December 2013. (a) Shows the flight path of the balloon (ascent in black, descent in grey), launched from Reading, UK. (b) demonstrates the presence of a low-level cloud layer widespread over most of the UK as measured by the AVHRR satellite (IR channel 4) at 1027 UTC, the same time as balloon launch time. Temperature and RH measured by the radiosonde are shown in (c) and (d), and data from the cloud and charge sensors shown in (e) and (f). Note that the visual range data are plotted on a log scale. Black shows the ascent, grey the descent through the same cloud layer 105 km from the launch point. Hollow black points in (f) denote charge values where the charge sensor saturated, therefore these values are a lower estimate of the charge in this region.

with the location of the lower and upper cloud edges clearly at 0.85 and 1.2 km respectively. Inside the cloud the visual range measured by the optical sensor decreases to 120 m (from >1000 m outside the cloud), and the solar radiation increases as the sensor travels upwards through the cloud layer, consistent with the decrease in optical depth. Figure 2(d) demonstrates space charge of up to $\pm 160\,\mathrm{pC\,m^{-3}}$ at both the upper and lower cloud edges, with very little charge in the middle of the cloud. The fact that the charge is concentrated in narrow layers at these cloud edges suggests that the mixing processes removing the charge occur at a lesser rate than the charging rate. In addition, the opposite polarity of charging between the upper and lower cloud boundaries (positive at cloud top, and negative at cloud base), in this case, agrees well with that predicted by the theory outlined in section 2.

The conductivity profile calculated from the estimation of Z_d and Eqs (4)–(6) is plotted in Figure 2(c), where it is seen that the presence of the cloud layer decreases the conductivity substantially (from approx. 10 to 2 fS m^{-1} from outside the cloud to inside), generating the expected vertical gradient in conductivity on the horizontal cloud edges. Also shown in Figure 2(c) is the estimated potential gradient profile through the cloud layer, which is calculated from the derived σ_t profile and Eq. (2), assuming that J_c is constant through the cloud layer (with $J_\mathrm{c} = 2\,\mathrm{pA\,m^{-2}}$). Note the similarity in the mean structure between the theoretical profiles in Figure 1 and the measured ones in Figure 2. Finally, the predicted cloud-edge space charge, shown in Figure 2(d) in grey, can be calculated from Eq. (3), again with $J_\mathrm{c} = 2\,\mathrm{pA\,m^{-2}}$, and using σ_t calculated from Eq. (6). Figure 2(d) also depicts the space charge measured directly by the charge sensor (in black), demonstrating good agreement between the locations of the predicted and measured charge layer, as well as the polarity. In this cloud layer, both the predicted and observed charge is located at the cloud-edge regions, where there is a vertical gradient in cloud-droplet number and size and therefore a conductivity gradient. It should be noted that exact agreement between the measured and theoretical profiles is not expected as the theory is based on a very simple (and static) view of clouds, and does not incorporate any vertical mixing which is known to exist in stratiform clouds (e.g. Shupe *et al.*, 2008). The magnitude of the calculated charge is somewhat smaller than that measured, but this varies with the assumptions made in Eqs (3)–(6), unlike the location of the charge layers, which depends solely on the location of the vertical conductivity gradient and therefore the vertical gradient in cloud droplet concentration. This sensitivity can be illustrated by perturbing the assumed values: increasing the value of J_c from 2 to 3 pA m^{-2} and decreasing q_i from 2 to 1 cm^{-3} s^{-1} increases the maximum predicted space charge from 37 to 111 pC m^{-3}.

4.2. *Horizontal distribution of charge within cloud layer*

As the vertical current flows throughout all fair-weather regions of the atmosphere, cloud-edge charging is expected across the entire horizontal extent of an extensive layer cloud. Preliminary experimental evidence for this was given in Rycroft *et al.* (2012) and is further supported here. Figure 3 shows data from an ascent and descent of an instrumented balloon through the same stratiform cloud layer, measured 105 km apart. Figure 3(a) shows the Global Positioning System (GPS) derived location of the balloon during its ascent from Reading (black) and descent (grey), and Figure 3(b) an infrared satellite image showing large-scale low-cloud coverage of the southern United Kingdom at the time of the balloon launch. Figure 3(c)–(f) show both ascent (black) and descent (grey) data from the instrumented balloon flight, whereby a cloud layer exists between 0.7 and 1 km (the lower part of the descent data is missing due to loss of the radiosonde signal close to the ground). This comparison demonstrates that all four profiles of temperature, RH, visual range and charge are similar between ascent and descent, with a slight lowering of the cloud top on the descent compared with the ascent. The charge sensor's response became saturated at its maximum value on both the ascent and descent stages of the flight at the cloud top (red points), suggesting a very large concentration of positive charge near the upper cloud edge. For this particular flight, saturation of the charge sensor would have occurred at approximately 200 pC m^{-3}, therefore it

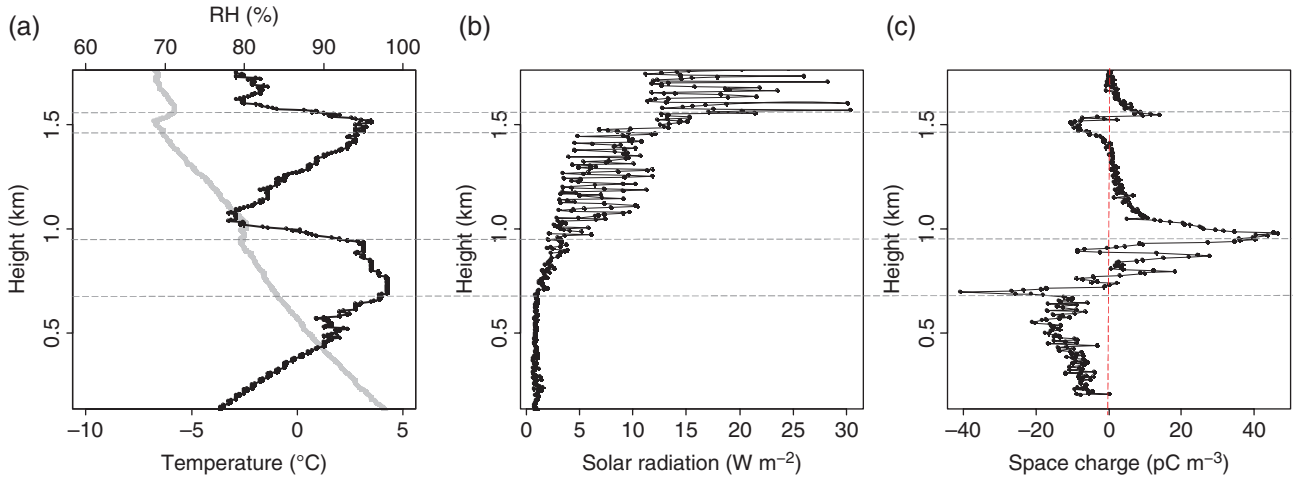

Figure 4. Vertical profile from an instrumented balloon flight through multiple stratiform cloud layers, launched from Reading on 8 February 2013. (a) Temperature and RH measured by the radiosonde, (b) solar radiation measured by the passive cloud sensor, (c) space charge measured by the charge sensor. Grey dashed lines denote approximate heights of cloud base and top.

is likely that the charge at cloud top exceeded this value. In contrast there is little evidence of a charge layer at the cloud base. The asymmetry in charge between cloud base and top is likely to be related to the large temperature inversion (of 10 °C), which leads to a particularly strong gradient in the visual range at cloud top (Figure 3(e)). From Eq. (3), this sharp thermodynamic transition from cloudy to clear air will result in a strong gradient in conductivity at the cloud top, with the expectation of substantial positive space charge accumulations; this is supported by the charge data shown in Figure 3(f). The substantial variability in the charge within the main body of the cloud (up to $\pm 100\,\mathrm{pC\,m^{-3}}$ which is larger than on most of the flights observed), with a gradual transition from positive to negative charge as cloud base is approached, may provide an explanation for the lack of a well-defined charge layer at cloud base, despite a clear gradient in visual range at cloud base. It is possible that downward mixing of the large amount of positive charge at cloud top acts to neutralise some of the negative charge at the cloud base, thus resulting in only slightly negative values towards the base of the cloud layer. Regardless of the explanation for the unusual charging behaviour, the existence of substantial charge at a similar height in the cloud but widely horizontally separated therefore confirms that cloud-edge charging is a horizontally widespread phenomena.

4.3. *Multiple cloud layers*

An interesting case of cloud-edge charging occurs when multiple, vertically displaced but overlapping cloud layers exist. Figure 4 shows vertical profiles from an instrumented balloon flight through two distinct cloud layers between 0.7–1.0 and 1.4–1.6 km (visual range was not available on this flight). Figure 4(c) demonstrates the presence of bipolar space charge in both layers, each with positive charge at cloud top and negative charge at cloud base, in agreement with the theory set out in section 2. The magnitude of the space charge in the upper cloud layer is much smaller than that in the lower cloud layer, which is likely related to a shallower conductivity gradient between clear and cloudy air in the upper cloud layer. This is likely to result from (i) differences in the cloud droplet profiles between the two clouds, with lower liquid water content expected in the upper cloud layer and (ii) an increase in the ion production rate in the upper cloud layer which acts to reduce the conductivity gradient (as modelled by Zhou and Tinsley (2007)). The effect of variations in ionisation rate on cloud-edge charging is discussed more fully in section 5. Nevertheless, the presence of space charge in both cloud layers confirms the continuity of current density through the upper cloud layer to the layer below, allowing the distinct cloud layers directly above each other to both become charged at their horizontal boundaries.

4.4. *Summary of all stratiform cloud flights*

Section 4.1 demonstrates a typical example of a stratiform layer cloud and the parameters measured by the specially instrumented radiosondes. The current section summarises the 22 different stratiform cloud layers sampled to date in order to quantify the variability between different cloud layers. The properties of the 22 stratiform cloud layers analysed are summarised in Table 1.

Table 1 demonstrates that the range of cloud-base heights sampled was from 475 to 4838 m, with a median height of 1367 m, with cloud depths (i.e. cloud-top height minus cloud-base height) ranging from the shallowest cloud layer of 86 m to the deepest of 1700 m (median cloud depth 285 m). The mean space-charge density in each cloud layer varied between 2 and $43\,\mathrm{pC\,m^{-3}}$, with a median of $16\,\mathrm{pC\,m^{-3}}$, with the maximum space-charge density in each cloud layer ranging from 10 to $253\,\mathrm{pC\,m^{-3}}$ (median $= 109\,\mathrm{pC\,m^{-3}}$). These values are calculated from the magnitude of the charge only, as taking the polarity into account results in values very close to zero due to the presence of opposite polarity charge at cloud base and cloud top. Figure 5 shows the variability in the space charge inside each of the 22 cloud layers in more detail, with each cloud layer plotted as an individual boxplot. The magnitude of space charge encountered during these flights is in agreement with previously reported values of stratiform cloud charge, which is typically found to be up to $1000\,\mathrm{pC\,m^{-3}}$ (e.g. Imyanitov and Chubarina, 1967; Nicoll and Harrison, 2009b, 2010; Nicoll, 2013).

Figure 2 presents measurements from an individual cloud/charge sensor flight through a stratiform cloud, which demonstrates agreement with theoretical expectations in terms of the location and polarity of the cloud-edge charge layers; however, the boxplots in Figure 5 show that considerable variability in charge can exist between different cloud layers. Figure 6 further demonstrates the variability between different cloud layers by showing the individual vertical profiles from 16 of the 22 stratiform clouds sampled, normalised by the measured cloud depth. Only clouds with mean altitude <3 km were selected as these lie within the typical altitude for stratocumulus clouds, and below this altitude the ion production rate varies less with height than at higher altitudes (see section 5.2). Figure 6(a) shows the in-cloud visibility as calculated from measurements from the cloud-droplet sensor using the method explained in section 3.1, and Figure 6(b) the space-charge density measured by the charge sensor. There is obvious variability in both the shape of the vertical profiles and magnitude of the space charge between individual cloud layers. It is therefore useful to consider the average profile through a stratiform cloud layer (Figure 6(c) and (d)). Figure 6(d) demonstrates that, as in the case of the individual cloud layer shown in Figure 2, on average, positive charge exists

Table 1. Details of cloud and charge sensor balloon flights through stratiform clouds from 2013 to 2015.

Cloud number	Date	Location	Mean cloud height (m)	Cloud depth (m)	Mean space charge (pC m^{-3})	Max. space charge (pC m^{-3})
1	22 April 2013	Reading	1534	446	39 ± 7	204
2	3 July 2013	Reading	1846	227	23 ± 6	143
3	4 July 2013	Reading	735	640	43 ± 6	253
4	31 July 2013	Reading	790	622	30 ± 5	200
5	16 August 2013	Reading	720	242	29 ± 6	153
6	16 August 2013_2	Reading	1200	90	18 ± 6	151
7	23 August 2013	Reading	4553	306	5 ± 1	32
8	31 October 2013	Reading	2522	333	9 ± 3	148
9	18 November 2013	Reading	1146	328	16 ± 4	174
10	18 November 2013_2	Reading	4197	135	2 ± 1	10
11	2 December 2013	Reading	1039	174	19 ± 4	97
12	3 December 2013	Reading	801	374	21 ± 4	172
13	27 May 2014	Hyytiala	4838	163	9 ± 2	75
14	27 May 2014_2	Hyytiala	1849	208	16 ± 5	104
15	29 May 2014	Hyytiala	3311	120	29 ± 6	113
16	29 May 2014_2	Hyytiala	3907	289	11 ± 3	133
17	30 May 2014	Hyytiala	2345	86	4 ± 13	52
18	30 May 2014_2	Hyytiala	499	178	23 ± 8	127
19	20 February 2015	Halley	1011	570	6 ± 1	42
20	21 February 2015	Halley	974	577	13 ± 1	92
21	6 March 2015	Halley	475	281	5 ± 1	32
22	6 March 2015	Halley	3067	1700	4 ± 1	102
Median			1367	285	16	120

The mean cloud height is the height of the centre of the cloud and the cloud depth is the difference in height between cloud base and top. The mean and maximum values of space charge are calculated from the magnitude of the in-cloud space charge for each cloud layer. The uncertainty in the mean charge is two standard errors on the mean values which represents the 95% confidence interval. Balloons which encountered several different layers of stratiform cloud on the same flight are denoted by '_2' in the flight date. NB: All data are from the ascent stage of the flight.

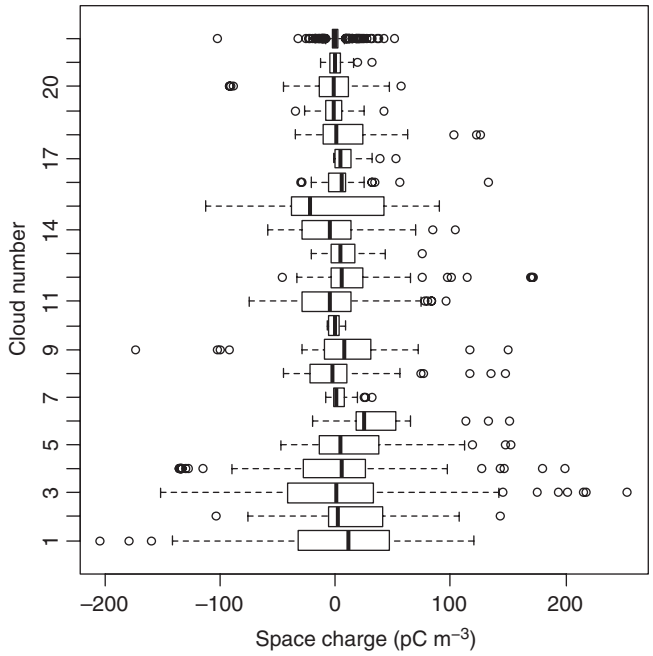

Figure 5. Boxplot of the space-charge distributions within each of the 22 studied cloud layers described in Table 1. The black solid line denotes the median of the distribution and box boundaries the interquartile range (IQR). Whiskers extend to +/−1.5 IQR.

at the cloud-top region, and negative charge in the cloud base. At the cloud top, the maximum mean charge is +32 pC m^{-3}, and at the base −24 pC m^{-3}, suggesting an asymmetry between cloud top and cloud base. The theoretical expectation is that this results from the vertical conductivity gradient, which in general is larger at cloud top than in the base (Harrison *et al.*, 2015), and discussed in more detail here in section 5.1. It is also interesting to note that, on average, the negatively charged region is relatively shallow and rapidly reaches a maximum value (at ∼20% cloud depth fraction), whilst the positively charged region is more vertically extensive (from 40to 90% of the cloud depth fraction). The fact that charge is observed away from the upper and lower cloud boundaries is likely to be due to mixing of charge through vertical motion from updraughts and downdraughts within the cloud volume. Although the stratiform nature of the clouds will minimise vertical motions, local variability and updraughts of up to 1 m s^{-1} nevertheless occur (e.g. Peng *et al.*, 2005). An asymmetry in the vertical extent of updraughts compared with downdraughts will result in different mixing profiles between cloud top and cloud base, which would influence the vertical extents of average positive and negative charge regions. Although the polarity of the average vertical space-charge profile agrees with theoretical predictions, on an individual cloud-to-cloud basis, considerable variability exists. This was originally documented by Imyanitov and Chubarina (1957) in a series of aircraft flights measuring electric field, E_z, from which the space-charge profiles could be derived using Eq. (1). They found that only 41% of 70 flights contained positive charge in the upper regions and negative charge in the base, with a mean space-charge density of 7.3 pC m^{-3} in the upper part, and −5.3 pC m^{-3} in the lower part. Similarly to Imyanitov and Chubarina (1967), the instrumented balloon flights from Reading, Hyytiala and Halley find that 57% of the 22 sampled stratiform clouds contain positive charge in their upper regions, and negative charge in the lower regions, whilst only 5% (one flight) have an inverted charge polarity structure (i.e. negative charge at top and positive in base). Thirty-three per cent of cloud layers contained positive charge at both cloud top and base, and 5% (i.e. one flight) negative charge at cloud top and base. Thus, on average the charge structure within low-level stratiform clouds agrees with that predicted by theory, but individual clouds may not. This is likely to be attributable to the oversimplification of cloud-edge charging theory, which does not take into account the dynamical motions within a cloud. For example, the existence of entirely positively charged clouds may be due to vertical mixing processes which act to transport positive charge downwards into the base of the cloud. The observed asymmetry between cloud-top and cloud-base charge could hypothetically cause positive charge to dominate over the negative, thus leading to a net positive charge throughout the cloud. The extent to which the theory holds for the set of measured layer clouds will be examined in the next section.

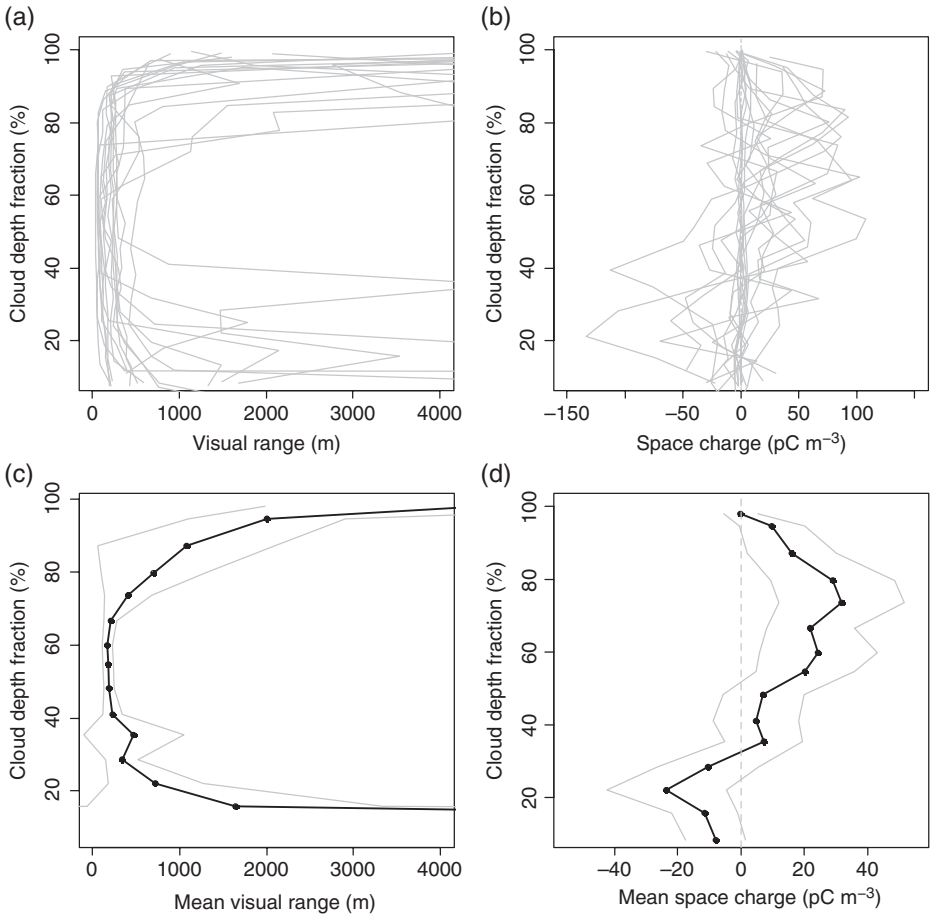

Figure 6. Profiles from 16 cloud and charge sensor balloon flights through stratocumulus clouds with height <3 km. (a) and (b) Individual profiles from flights, (c) and (d) average profiles calculated from the 16 flights. (a) and (c) Visibility derived from cloud sensor, (b) and (d) space charge measured by the charge sensor. The *y*-axis denotes height normalised by cloud depth, found by dividing each cloud layer into 15 evenly spaced altitude layers, where 0% denotes cloud base and 100% cloud top. The data points in (c) and (d) are calculated from the mean of the variables in each of the 15 altitude layers. Grey solid lines in (c) and (d) show two standard errors on the mean values.

5. Factors controlling cloud-edge charging

Equation (3) describes the cloud-edge charge in solely steady-state electrostatic terms, specifically the variation with height of the air conductivity and the local vertical conductivity gradient. This section will now deal with each of these factors in turn.

5.1. *Conductivity gradient*

One property which shows great variability between clouds is the thickness of the transition zone between clear air and the horizontal cloud edge, which is directly related to the vertical gradient in conductivity, and also the generation of space charge in accordance with Eq. (3). A direct measurement of the cloud-edge transition zone thickness can be obtained from the optical measurements made by the cloud-droplet sensor. An example of a particularly narrow (or 'sharp') cloud-edge transition zone is shown in the cloud layer in Figure 3, where the optical transition from cloud to clear air at the cloud top takes place over a depth of 30 m. In this cloud layer the space charge within the cloud top is co-located exactly where the optical cloud changes occur, with the magnitude of the space charge increasing as the visibility decreases. The charge at cloud top in this particular cloud layer is so large that it saturated the charge sensor (giving a lower limit of charge as $>200\,\mathrm{pC\,m^{-3}}$). The same cannot be said for the cloud-base region, however, which has a much less distinct change from clear to cloudy air, and hence no appreciable amount of space charge is located in the cloud-base region. For all of the 22 stratiform clouds studied here, the nature of the cloud-top and cloud-base transitions, with the cloud-top transition extending vertically over a narrower region, is consistent between clouds. This is expected from the often sharp temperature inversion in the cloud-top region, which acts as a lid to further upward motion, which is not present in the cloud-base region. The magnitude of the charge which accumulates at horizontal cloud edges is therefore constrained by thermodynamic processes.

Figure 7 shows boxplots of the cloud-edge transition zone thickness, visibility gradient and space charge measured at both horizontal cloud edges of cloud top and cloud base for 16 of the cloud layers with altitudes <3 km. The cloud base was identified on the basis of determining where the optical cloud-droplet sensor voltage began increasing, and cloud top from where it was decreasing. The cloud-edge transition zone thickness was also selected on this basis. It is seen that in general, the cloud-edge transition zone is narrower at cloud top (median depth 72 m) than cloud base (median depth 128 m). Similarly the gradient in visibility (which is related to the cloud-droplet concentration and conductivity by Eqs (5)–(7)), is also larger at cloud top (42 m/m) than cloud base (21 m/m). In agreement with this, the magnitude of the space charge in cloud-top regions is also greater at cloud top (median $45\,\mathrm{pC\,m^{-3}}$) than at cloud base (median $29\,\mathrm{pC\,m^{-3}}$), demonstrating an asymmetry in charge between cloud top and cloud base. It follows that the largest magnitude of cloud-edge charging will occur in stable stratified layers with sharp edges and little vertical mixing. These properties are typical of marine stratocumulus, which are characterised by strong temperature inversions at cloud top.

5.2. *Conductivity and altitude variation*

Conductivity varies substantially with height because of the variation in cosmic ray ion production, and contribution from radon near the surface, therefore to investigate the height dependence of cloud-edge charge it is first necessary to determine

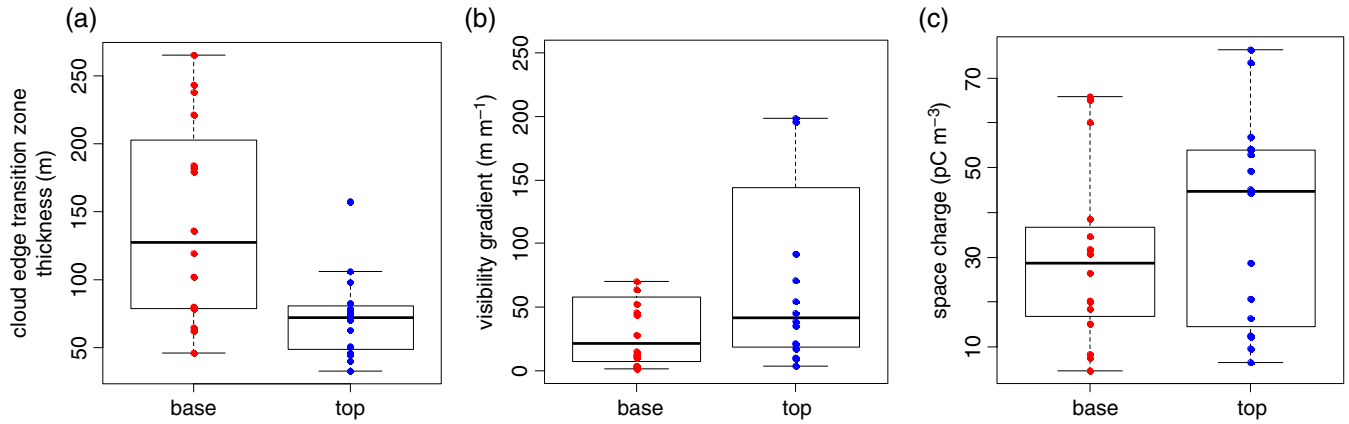

Figure 7. (a) Vertical extent of transition region between cloudy and clear air, (b) gradient in visibility at cloud edge measured by cloud sensor, (c) magnitude of space charge measured by charge sensor. Left-hand boxplots represent cloud base (red) and right-hand plots cloud top (blue). Data are averages over cloud top/base region, where each point represents one cloud edge and only include cloud layers <3 km altitude. Cloud-base regions are selected on the basis of when the optical cloud-droplet sensor voltage was increasing, and cloud top when it was decreasing.

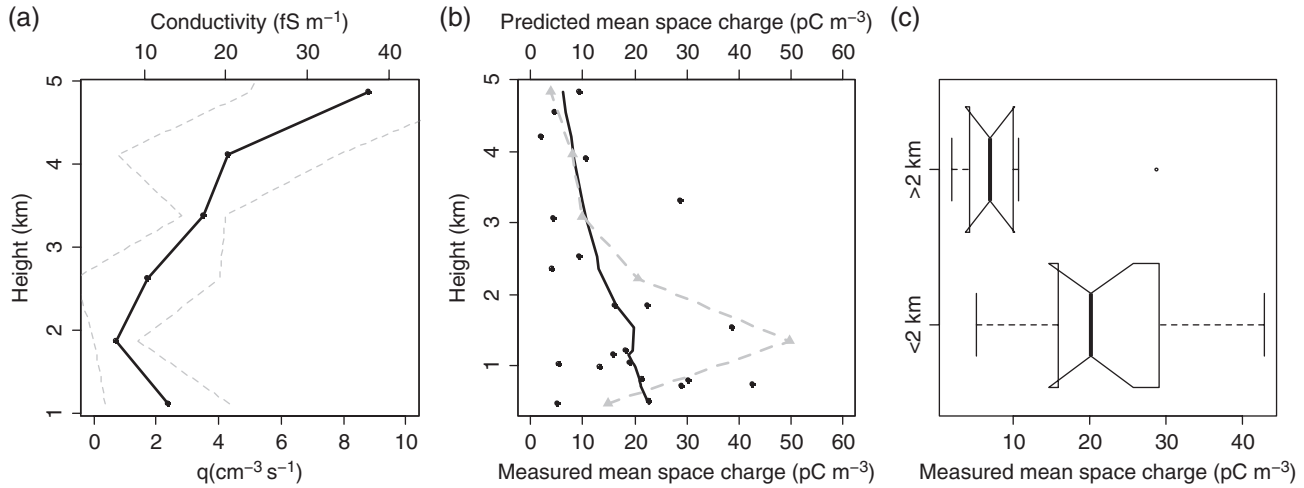

Figure 8. (a) Average vertical profile of ionisation rate measured by a balloon-borne Geiger sensor and corresponding conductivity profile calculated from Eq. (6) for Reading, Hyytiala and Halley between 2013 and 2015. Grey lines denote two standard errors on the mean values. (b) Magnitude of the mean in-cloud space charge (grey dotted line), predicted as a function of height, using the average cloud-droplet profile of the case in Figure 2, and the ambient conductivity profile in (a), and measured mean space charge (absolute values) from all 22 cloud layers at Reading, Hyytiala and Halley (black points and black line, which shows a lowess fit to the data points). (c) Boxplot of measured mean space-charge values separated into two cloud height ranges, with mean cloud height <2 (14 cloud layers) and >2 km (8 cloud layers). The edges and line in the centre of the boxes show the upper and lower quartiles and the median. Notches indicate the 95% confidence limits on the median, and whiskers extend to 1.5 times the interquartile range.

the vertical profile of conductivity. Conductivity profiles can be measured directly e.g. by a Gerdien-type sensor (e.g. Nicoll and Harrison, 2008) or indirectly by measuring the ion production rate. Measurements showing the ion production rate variation with height have been presented by Harrison *et al.* (2014) using the balloon-borne Geiger sensor described in section 3.1. In this study, measurements of vertical profiles of ionisation rate have been obtained at all three cloud measurement sites of Reading, Hyytiala and Halley, which allow the average vertical ion production rate profile from the surface up to 5 km for all of the sites together to be found, as well as the clear-air conductivity profile (shown in Figure 8(a)).

To determine the effect of cloud height on the generated space charge, an estimate of the in-cloud conductivity profile has been derived from the cloud-droplet profile of the cloud shown in Figure 2, typical of the average cloud profile, and Eq. (6). The predicted magnitude of the mean space charge in the cloud is then calculated from Eq. (3), using the calculated conductivity values from Figure 8(a). This is then compared with the measured mean value (magnitude) of space charge measured from all 22 cloud layers at the three measurement sites (where the predicted and measured values of charge are shown as the grey line and black points in Figure 8(b) respectively). It is seen that the predicted space charge follows closely the inverse variation in ionisation rate with height, with a reduction in ionisation at approximately 1 km where the radon contribution falls off. Although the same variation is not so evident in the measured space-charge values, the black line depicts a lowess (locally weighted scatterplot regression) fit to the data which does demonstrate elevated space-charge values in the lowest 1.5 km, which falls off rapidly with increasing height. This is supported by the boxplot in Figure 8(c) which divides the measured mean space-charge values according to the height of cloud in which they were measured. It is clear that there is a statistically significant difference (at the 95% confidence level) in the mean space charge measured in clouds below and above 2 km, with lower altitude clouds being more highly charged. The median of the mean space-charge distribution for the low altitude (<2 km) clouds is 20.2 and 7.0 pC m^{-3} for the higher altitude clouds (>2 km). The ratio of these two space-charge values is 2.9 which is very similar to the ratio of mean conductivity (=2.8) below and above 2 km from Figure 8(a). There is also a noticeable difference in the range of the space-charge values between the two altitude ranges, with the interquartile range (IQR) = 11.5 pC m^{-3} for low altitude clouds compared to IQR = 5.4 pC m^{-3} for the higher altitude clouds, potentially related to the smaller magnitude of space charge in the higher altitude clouds. The data shown in Figure 8 thus support the hypothesis that the droplet charging effect is greatest for low altitude stratiform cloud, which would be particularly so over the oceans, where any radon contribution to the total ionisation rate is negligible.

Substantial scatter in the data points is expected as a number of factors influence the space-charge generation in clouds in

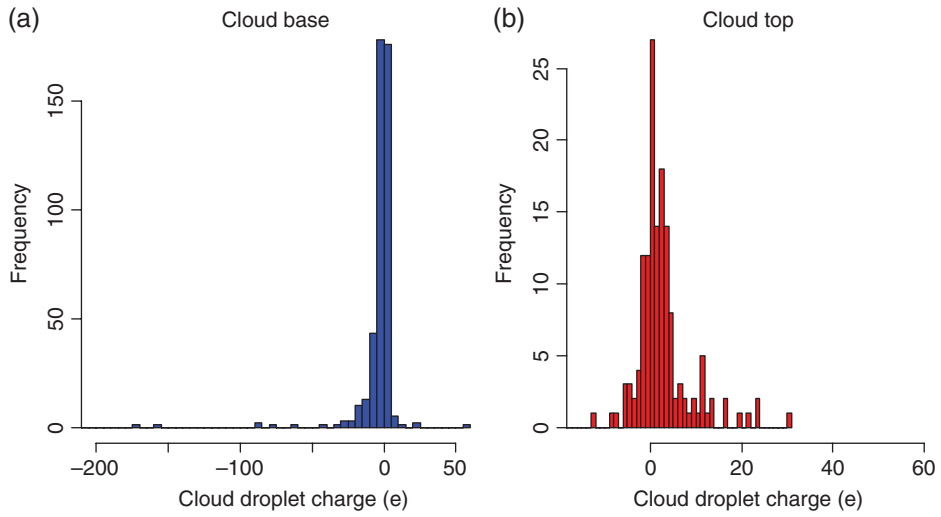

Figure 9. Histograms of individual cloud-droplet charges (in units of elementary charge, e), calculated from measured space charge and calculated equivalent cloud-droplet number concentration (assuming cloud droplets are monodisperse with 10 µm diameter), for (a) cloud base and (b) cloud top for 16 stratiform cloud layers <3 km altitude. (a) Contains 444 data points and (b) 147 points, since the cloud-top region is typically much shallower than the base.

addition to the conductivity profile. No allowance has been made here for differences in cloud-edge transition zone thickness between low altitude and high altitude clouds, which may result from dynamical changes between the different cloud altitudes. Further, it should be noted that the assumption of using the average cloud-droplet profile for all altitudes of cloud between 1 and 5 km is another potential source of variability, which also does not take account of dynamical changes in clouds that typically occur with altitude changes. Although it would be preferable to repeat this analysis to take these points into consideration, as well as to plot the data from each of the three measurement sites individually, the small number of data points limits the statistical analysis possible.

6. Cloud-droplet charging

The results shown in section 4 combined with theory provide strong evidence that widespread charging occurs within the edge regions of stratiform cloud layers. Simultaneous charge and cloud-droplet measurements also indicate that the charge is likely to reside primarily on the cloud droplets, since charge is typically observed to be present mainly within the region where the visual range indicates that cloud is present. As mentioned in section 1, there are several physical consequences associated with the charging of cloud droplets, including modification of droplet–particle interactions and droplet activation; however, the extent to which the droplet behaviour is influenced depends on the magnitude of the droplet charge. Since most of the space charge within a cloud will reside on cloud droplets it is possible to represent the measured space-charge density values discussed in section 4 in terms of elementary charges per droplet, rather than charge per unit volume. If the charge density ρ is assumed to be partitioned equally between cloud droplets with concentration, Z_d, the mean number of elementary charges per droplet j is given by

$$j = \frac{\rho}{Z_d e}. \tag{7}$$

Summary histograms of individual cloud-droplet charges are shown in Figure 9 for (a) cloud-base and (b) cloud-top regions, for all 16 cloud layers with altitude <3 km (with cloud base and top selected on the basis of changes in the optical cloud-droplet sensor response, as for Figure 7). For each cloud layer, Eq. (7) was applied to the measured space-charge values, together with the calculated equivalent cloud-droplet number concentration profile (calculated from the cloud sensor measurements and assuming that cloud droplets are monodisperse with 10 µm diameter). At cloud base, the range of cloud-droplet charges from Figure 9(a) is −270 to 57e, with median −0.4e, whilst at cloud top, droplet charges range from −26 to 31e, with median 1.4e. Since the droplet charge is calculated directly from the space-charge measurements, overall the droplet charges are largely negative at cloud base and positive at cloud top, with a slight asymmetry between the two in that cloud-droplet charges at the cloud top are slightly larger than in the base.

7. Discussion

This work presents the first quantitative comparison of multiple observations of stratiform cloud-edge charging from multiple sites. Although general agreement between observations and theory in the location and polarity of the charge layers is found on average across all the soundings, substantial local differences are apparent in individual clouds. The results discussed here therefore demonstrate that cloud-edge charging is dependent on both the dynamical properties of the cloud as well as the background electrical environment. Turbulence and updraughts and downdraughts inside the cloud layer will act to mix the charge generated at the cloud edges, and the presence of ice as well as varying aerosol concentrations (which are not considered here) are also likely to play a role in the resultant charge profile.

The confirmation of the asymmetry in charging between cloud base and top is an important factor which has hitherto not been included in modelling studies of layer-cloud electrification, and has potentially important consequences for larger charging of droplets at cloud top than base. In terms of the implications for cloud microphysical processes, the magnitude of the estimated droplet charges (from a few e per droplet to 270e) are large enough to affect droplet–droplet collision processes, but likely not droplet activation, which is thought to require charges of ∼1000e. Harrison *et al.* (2015) describes the increased collision rate between small and large droplets when both droplets are equally charged through an increase in the collision efficiency, which results from the mutual attraction of the droplets from the electrical image force. This occurs even when the droplets have the same polarity of charge (as would typically be the case in an unmixed cloud layer), and will be most dominant for droplets <2 µm, likely resulting in a depletion in the number concentration of small droplets.

Over-range of the charge sensor occurred on one flight (shown in Figure 3), demonstrating that space-charge regions >200 pC m^{-3} can exist within stratiform clouds. Measurements from the optical cloud-droplet sensor presented here provide a more realistic value of cloud-edge depth of ∼100 m than that previously used in modelling studies (e.g. 11 m in Zhou and

Tinsley (2007)), and the large variability observed in the charge profiles on an individual cloud-to-cloud basis suggest that the simple modelling approach adopted up to now needs to be extended for future studies. These therefore present a unique dataset of in-cloud stratiform charge measurements which can help to inform future modelling studies of cloud-droplet charging effects on cloud microphysics (e.g. Zhou and Tinsley, 2012; Tinsley and Leddon, 2013; Harrison *et al.*, 2015).

Although not considered in detail here, variations in the air–Earth conduction current may also contribute to some of the variability in cloud-edge charging since it is the flow of this vertical current through cloud layers which leads to the accumulation of space charge at cloud edges. J_c is controlled by a number of factors internal to Earth's climate system, which are mainly associated with the Global atmospheric Electric Circuit (GEC). This is driven by global thunderstorm activity, therefore changes in thunderstorm output current and lightning activity (which are known to be linked to surface temperature changes and global weather patterns such as El Niño/Southern Oscillation (ENSO) (Williams, 1992; Harrison *et al.*, 2011)) will act to increase or decrease J_c. Variations in the vertical conductivity profile, such as from volcanic eruptions, or even the presence of cloud layers themselves (e.g. Nicoll and Harrison, 2009a; Zhou and Tinsley, 2010; Baumgaertner *et al.*, 2014) also play a role in modulating J_c. Conductivity variations also occur, more dominantly, through external factors such as changes in the GCR flux (e.g. decreases in global ionisation rates of up to 10% can occur during Forbush decreases, typically associated with explosive events on the Sun), and also from solar proton events. Understanding the effects of space weather on the GEC and therefore J_c should therefore remain an area of active research, particularly as solar disturbances have the potential to affect cloud-edge charging through the mechanism discussed here (see Nicoll (2014) and Mironova *et al.* (2015) for recent reviews). There is no doubt that assessing the importance of the role that J_c plays in modulating cloud-edge charging is difficult to do. Measurements of J_c are sparse, and because significant variability in cloud-charge profiles exists between individual cloud layers, a larger statistical sample of cloud-charge data is therefore required to properly assess this important factor.

8. Conclusions

These results represent the first multiple-site comparison of non-thunderstorm cloud charge, and the first study to undertake simultaneous high vertical resolution measurements of cloud-droplet and charge properties in multiple cloud layers and compare them with theoretical charging expectations. The cloud and charge data demonstrate unequivocally that all stratiform clouds can be expected to contain charge at their upper and lower boundaries to a varying extent, due to vertical current flow in the Global atmospheric Electric Circuit. On average, charge is found near upper and lower cloud edges and the cloud-edge charge polarity (positive at cloud top and negative at cloud base) agrees with theory, but large variations in both location and polarity of charge are observed within individual cloud layers, likely due to dynamical processes within the clouds, which are at present not included in theoretical models of cloud-edge charging.

The results also demonstrate that a combination of cloud thermodynamics with the background electrical conditions contribute to the magnitude of cloud-edge charging in terms of the 'sharpness' of the cloud-edge transition zone thickness. This is observed in terms of an asymmetry between cloud top and base charge, typically with larger charge observed at cloud top (32 compared to 24 pC m^{-3} in the cloud base) due to the more rapid transition from cloudy to clear air which often occurs due to a significant temperature inversion in the cloud-top region.

Finally, the difference in cloud charge robustly observed between low altitude (<2 km) and higher altitude stratiform clouds (2–5 km) demonstrates the important role of cosmic ray ionisation in the cloud-edge charging process, if the other edge properties of clouds remain unchanged. This confirms the theoretical expectation that layer-cloud electrification will be at its greatest for low-level clouds.

Acknowledgements

NERC (Natural Environment Research Council) grant NE/H002081/1 and STFC grant ST/K001965/1 supported the radiosonde sensor development. KAN also acknowledges an Early Career Fellowship of the Leverhulme Trust (ECF-2011-225), a NERC Independent Research Fellowship (NE/L011514/1), NERC Collaborative Gearing Scheme (CGS) grant and ACTRIS TransNational Access funding from the European Union Seventh Framework Programme (FP7/2007-2013) under grant agreement no. 262254. Logistics support for Hyytiala launches was **supported by the Office of Biological and Environmental Research of the US Department of Energy as part of the Atmospheric Radiation Measurement (ARM) Climate Research Facility, an Office of Science user facility.** Technicians in the Department of Meteorology at the University of Reading assisted with sensor assembly and the majority of the balloon launches. Assistance with additional balloon launches was provided by ARM AMF2 technicians at Hyytiala, and staff at the British Antarctic Survey research station at Halley. The satellite image in Figure 7 is courtesy of NERC Satellite Receiving Station, Dundee University, Scotland: http://www.sat.dundee.ac.uk/. The balloon flight data used in the analysis are archived through the University of Reading Data repository at http://dx.doi.org/10.17864/1947.38.

Appendix A: Effective area of charge sensor

The balloon-borne charge sensor used to provide the in-cloud charge measurements employs an approximately spherical electrode connected to a sensitive electrometer, and primarily responds to induced displacement currents generated by electric field changes as the sensor moves through the cloud layer. A full description of the sensor electronics is given by Nicoll (2013), with further details of the calculation of cloud space-charge given here.

The electrometer circuit comprises a current to voltage converter employing a T-network of resistors to synthesise a total effective resistance, $R = 2.4 \times 10^{11}\ \Omega$. The induced current, i, is related to the final output voltage of the electrometer circuit, V_{out}, by

$$i = \frac{V_{out}}{R}. \tag{A1}$$

To calculate the space-charge density, ρ, first consider the charge, Q, induced on a stationary sensor electrode due to the electric field. This is given by Gauss' law as

$$Q = -A_{eff}\varepsilon_0 E, \tag{A2}$$

where A_{eff} is the effective area of the electrode, i.e. the area of the conductor on which the field lines end, which is not necessarily the same as its geometrical surface area. If the sensor is allowed to move, for example by ascending vertically through a cloud layer, the electric field will change, and the induced charge is no longer constant, causing an induced current, i, to flow, measured by the electrometer and given by

$$i = \frac{dQ}{dt} = -A_{eff}\varepsilon_0 \frac{dE}{dt} = \frac{V_{out}}{R}. \tag{A3}$$

For vertical motion on a free balloon with ascent rate w, the $\mathrm{d}E/\mathrm{d}t$ term in Eq. (A3) is

$$\frac{dE}{dt} = \frac{dt}{dz}\frac{dE}{dt} = \frac{1}{w}\frac{dE}{dz}, \tag{A4}$$

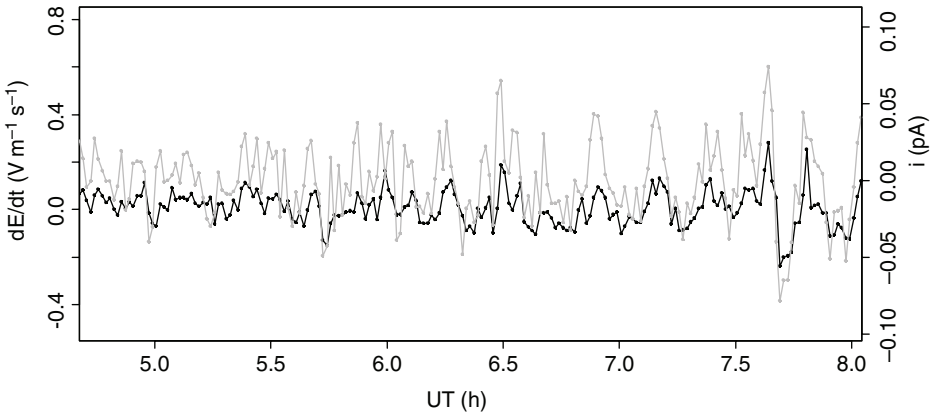

Figure A1. Time series of data from calibration of balloon-borne charge sensor in fog on Reading University Atmospheric Observatory (RUAO). The electric field change (dE/dt) measured by a commercial field mill (JCI 131) is shown in black and the corresponding current measured by the charge sensor as a result of the electric field changes shown in grey.

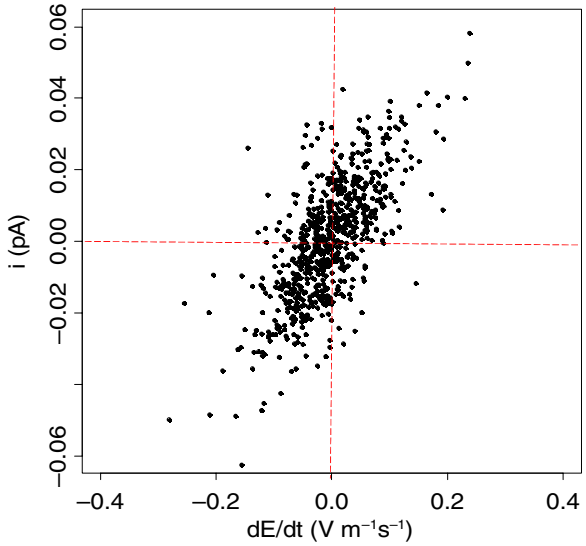

Figure A2. Calibration of balloon-borne charge sensor during fog-induced electric field changes. Sensor electrode current, i, is plotted against simultaneously measured rate of change of electric field (dE/dt) measured by a commercial field mill.

and therefore the current measured by the electrometer is related to the electric field gradient by

$$i = -A_{eff}\varepsilon_0 \frac{1}{w}\frac{dE}{dz}. \tag{A5}$$

From Eqs (1) and (A5) and substituting for the dE/dz term, it follows that the space charge, ρ, measured by the charge sensor is related to the measured current by

$$\rho = \frac{i}{A_{eff} w}. \tag{A6}$$

The unknown quantity in Eq. (A6) is the effective area term, A_{eff}. This can be determined from experimental calibration using Eq. (A3), by placing the charge sensor in a varying electric field which is known.

The experimental calibration was undertaken by measuring the atmospheric electric field in fog (using an electric field mill at the Reading University Atmospheric Observatory (RUAO)) and placing the charge sensor nearby. (The field mill was previously standardised for its form factor using the passive wire antenna method (Bennett and Harrison, 2006)). Fog typically causes the atmospheric electric field to increase and become variable thus generating a sufficiently large dE/dt with which to calibrate the charge sensor. Figure A1 shows a time series of the rate of change of electric field (measured by the field mill, in black) and the current measured by the charge sensor during a 3 h period of fog. The extremely good correlation between the two traces (Pearson correlation coefficient = 0.75) demonstrates that not only does the balloon charge sensor respond well to changes in electric field, and thus space charge, but its dE/dt response is very similar to that of the commercially available field mill. Figure A2 shows the relationship between the current measured by the charge sensor and dE/dt measured by the field mill.

The effective area of the charge sensor electrode can thus be found from a linear fit between i and dE/dt (Figure A2) as

$$i = -A_{eff}\varepsilon_0 \frac{dE}{dt}, \tag{A7}$$

from which it is calculated that $A_{\text{eff}} = 0.0196\,\text{m}^2$. This can be compared to the approximate surface area of a perfectly spherical electrode (with radius 0.6 cm), $A = 0.000452\,\text{m}^2$, i.e. approximately 43 times smaller than the effective area, which is reasonable considering the likely electric field distortion from the relatively complex geometry of the charge sensor electrode. The final space-charge value is then computed using A_{eff} above and Eq. (A6), using the local ascent rate in the cloud as found by the radiosonde height information.

References

Allee PA, Phillips BB. 1959. Measurement of cloud-droplet charge, electric field, and polar conductivities in supercooled clouds. *J. Atmos. Sci.* **16**: 405–410.

Baumgaertner AJG, Lucas GM, Thayer JP, Mallios SA. 2014. On the role of clouds in the fair weather part of the global electric circuit. *Atmos. Chem. Phys.* **14**: 8599–8610, doi: 10.5194/acp-14-8599-2014.

Bazilevskaya GA, Usoskin IG, Flückiger EO, Harrison RG, Desorgher L, Bütikofer R, Krainev MB, Makhmutov VS, Stozhkov YI, Svirzhevskaya AK, Svirzhevsky NS, Kovaltsov GA. 2008. Cosmic ray induced ion production in the atmosphere. *Space Sci. Rev.* **137**: 149–173.

Beard KV, Ochs HT, Twohy CH. 2004. Aircraft measurements of high average charges on cloud drops in layer clouds. *Geophys. Res. Lett.* **31**: L14111.

Blakeslee RJ, Mach DM, Bateman MG, Bailey JC. 2014. Seasonal variations in the lightning diurnal cycle and implications for the global electric circuit. *Atmos. Res.* **135–136**: 228–243.

Bennett AJ, Harrison RG. 2006. In situ calibration of atmospheric air conductivity instruments. *Rev. Sci. Instrum.* **77**: 016103.

Bennett AJ, Harrison RG. 2009. Evidence for global circuit current flow through water droplet layers. *J. Atmos. Sol. Terr. Phys.* **71**: 1219–1221.

Bohren CF, Huffman DT. 1983. *Absorption and Scattering of Light by Small Particles*. Wiley: New York, NY.

Gunn R. 1954. Diffusion charging of atmospheric droplets by ions and the resulting combination coefficients. *J. Meteorol.* **11**: 339–347.

Harrison RG. 2012. Aerosol-induced correlation between visibility and atmospheric electricity. *J. Aerosol Sci.* **52**: 121–126.

Harrison RG, Ambaum MHP. 2008. Enhancement of cloud formation by droplet charging. *Proc. R. Soc. A.* **464**: 2561–2573.

Harrison RG, Ambaum MHP. 2013. Electrical signature in polar night cloud base variations. *Environ. Res. Lett.* **8**: 015027, doi: 10.1088/1748-9326/8/1/015027.

Harrison RG, Carslaw KS. 2003. Ion–aerosol–cloud processes in the lower atmosphere. *Rev. Geophys.* **41**: 1012, doi: 10.1029/2002RG000114.

Harrison RG, Nicoll KA. 2014. Active optical detection of cloud from a balloon platform. *Rev. Sci. Instrum.* **85**: 066104, doi: 10.1063/1.4882318.

Harrison RG, Joshi M, Pascoe K. 2011. Inferring convective responses to El Niño with atmospheric electricity measurements at Shetland. *Environ. Res. Lett.* **6**: 044028, doi: 10.1088/1748-9326/6/4/044028.

Harrison RG, Nicoll KA, Lomas AG. 2012. Programmable data acquisition system for research measurements from meteorological radiosondes. *Rev. Sci. Instrum.* **83**: 036106, doi: 10.1063/1.3697717.

Harrison RG, Nicoll KA, Lomas AG. 2013. Geiger tube coincidence counter for lower atmosphere radiosonde measurements. *Rev. Sci. Instrum.* **84**: 076103, doi: 10.1063/1.4815832.

Harrison RG, Nicoll KA, Aplin KL. 2014. Vertical profile measurements of lower troposphere ionisation. *J. Atmos. Sol. Terr. Phys.* **119**: 203–210, doi: 10.1016/j.jastp.2014.08.006.

Harrison RG, Nicoll KA, Ambaum MHP. 2015. On the microphysical effects of observed cloud edge charging. *Q. J. R. Meteorol. Soc.* **141**: 2690–2699, doi: 10.1002/qj.2554.

Hirsikko A, Paatero J, Hatakka J, Kulmala M. 2007. The ^{222}Rn activity concentration, external radiation dose and air ion production rates in a boreal forest in Finland between March 2000 and June 2006. *Boreal Environ. Res.* **12**: 265–278.

HMSO, KL. 1982. *Handbook of Meteorological Instruments*. *Measurement of Visibility and Cloud Height*, Vol. **7**. Meteorological Office, Her Majesty's Stationery Office: London, UK.

Imyanitov IM, Chubarina EV. 1967. *Electricity of the Free Atmosphere*. Israel Program for Scientific Translations: Jerusalem, Israel.

Israel H. 1971. *Atmospheric Electricity*. Israel Program for Scientific Translations: Jerusalem, Israel.

Jones OC. 1957. 'Problems in atmospheric ionisation', PhD dissertation. University of Oxford, UK.

Jones OC, Maddever RS, Sanders JH. 1959. Radiosonde measurement of vertical electrical field and polar conductivity. *J. Sci. Instrum.* **36**: 24.

Khain A, Arkhipov V, Pinsky M, Feldman Y, Ryabov Y. 2004. Rain enhancement and fog elimination by seeding with charged droplets. Part I: Theory and numerical simulations. *J. Appl. Meteorol.* **43**: 1513–1529.

Klein SA, Hartmann DL. 1993. The seasonal cycle of low stratiform clouds. *J. Clim.* **6**: 1587–1606.

Koren I, Remer LA, Kaufman YJ, Rudich Y, Martins JV. 2007. On the twilight zone between clouds and aerosols. *Geophys. Res. Lett.* **34**: L08805, doi: 10.1029/2007GL029253.

Mach DM, Blakeslee RJ, Bateman MG. 2011. Global electric circuit implications of combined aircraft storm electric current measurements and satellite-based diurnal lightning statistics. *J. Geophys. Res.* **116**: D05201, doi: 10.1029/2010JD014462.

Miles NL, Verlinde J, Clothiaux EE. 2000. Cloud droplet size distributions in low-level stratiform clouds. *J. Atmos. Sci.* **57**: 295–311.

Mironova IA, Aplin KL, Arnold F, Bazilevskaya GA, Harrison RG, Krivolutsky AA, Nicoll KA, Rozanov EV, Turunen E, Usoskin IG. 2015. Energetic particle influence on the Earth's atmosphere. *Space Sci. Rev.* **194**: 1–96, doi: 10.1007/s11214-015-0185-4.

Nicoll KA. 2013. A self-calibrating electrometer for atmospheric charge measurements from a balloon platform. *Rev. Sci. Instrum.* **84**: 096107, doi: 10.1063/1.4821500.

Nicoll KA. 2014. Space weather influences on atmospheric electricity. *Weather* **69**: 238–241, doi: 10.1002/wea.2323.

Nicoll KA, Harrison RG. 2008. A double Gerdien instrument for simultaneous bipolar air conductivity measurements on balloon platforms. *Rev. Sci. Instrum.* **79**: 084502, doi: 10.1063/1.2964927.

Nicoll KA, Harrison RG. 2009a. Vertical current flow through extensive layer clouds. *J. Atmos. Sol. Terr. Phys.* **71**: 2040–2046.

Nicoll KA, Harrison RG. 2009b. A lightweight balloon-carried cloud charge sensor. *Rev. Sci. Instrum.* **80**: 014501, doi: 10.1063/1.3065090.

Nicoll KA, Harrison RG. 2010. Experimental determination of layer cloud edge charging from cosmic ray ionisation. *Geophys. Res. Lett.* **37**: L13802, doi: 10.1029/2010GL043605.

Nicoll KA, Harrison RG. 2012. Balloon-borne disposable radiometer for cloud detection. *Rev. Sci. Instrum.* **83**: 025111.

Peng Y, Lohmann U, Leaitch R. 2005. Importance of vertical velocity variations in the cloud droplet nucleation process of marine stratus clouds. *J. Geophys. Res.* **110**: D21213, doi: 10.1029/2004JD004922.

Phillips BB, Kinzer GD. 1958. Measurement of the size and electrification of droplets in cumuliform clouds. *J. Meteorol.* **15**: 369–374.

Rycroft MJ, Nicoll KA, Aplin KL, Harrison RG. 2012. Global electric circuit coupling between the space environment and the troposphere. *J. Atmos. Sol. Terr. Phys.* **90–91**: 198–211, doi: 10.1016/j.jastp.2012.03.015.

Shupe MD, Kollias P, Persson POG, McFarquhar GM. 2008. Vertical motions in Arctic mixed-phase stratiform clouds. *J. Atmos. Sci.* **65**: 1304–1322.

Tinsley BA. 2000. Influence of solar wind on the global electric circuit, and inferred effects on cloud microphysics, temperature and dynamics in the troposphere. *Space Sci. Rev.* **94**: 231–258.

Tinsley BA, Leddon DB. 2013. Charge modulation of scavenging in clouds: Extension of Monte Carlo simulations and initial parameterization. *J. Geophys. Res. Atmos.* **118**: 8612–8624.

Tinsley BA, Rohrbaugh RP, Hei M, Beard KV. 2000. Effects of image charges on the scavenging of aerosol particles by cloud droplets and on droplet charging and possible ice nucleation processes. *J. Atmos. Sci.* **57**: 2118–2134.

Twomey S. 1956. The electrification of individual cloud droplets. *Tellus* **4**: 445–451.

Williams ER. 1992. The Schumann resonance: A global tropical thermometer. *Science* **256**: 1184.

Wilson CTR. 1929. Some thundercloud problems. *J. Franklin Inst.* **208**: 1–12.

Zhou L, Tinsley BA. 2007. Production of space charge at the boundaries of layer clouds. *J. Geophys. Res.* **112**: D11203, doi: 10.1029/2006JD007998.

Zhou L, Tinsley BA. 2010. Global circuit model with clouds. *J. Atmos. Sci.* **67**: 1143–1156, doi: 10.1175/2009JAS3208.1.

Zhou L, Tinsley BA. 2012. Time dependent charging of layer clouds in the global electric circuit. *Adv. Space Res.* **506**: 828–842.